The HKU Scholars Hub   The University of Hong Kong   香港大學學術庫

Title	**X-RAY/GeV EMISSIONS FROM CRAB-LIKE PULSARS IN THE LMC**
Author(s)	**Takata, J; Cheng, KS**
Citation	**The Astrophysical Journal, 2016, v. 834 n. 1, p. 4:1-9**
Issued Date	**2016**
URL	**http://hdl.handle.net/10722/238696**
Rights	**The Astrophysical Journal. Copyright © American Astronomical Society, co-published with Institute of Physics Publishing, Inc.; This work is licensed under a Creative Commons Attribution-NonCommercial-NoDerivatives 4.0 International License.**

X-ray/GeV emissions from Crab-like pulsars in LMC

Takata, J.[1]

and

Cheng, K. S.[2]

takata@hust.edu.cn, hrspksc@hku.hk

ABSTRACT

We discuss X-ray and gamma-ray emissions from Crab-like pulsars, PSRs J0537-6910 and J0540-6919, in Large Magellanic Cloud. Fermi-LAT observations have resolved the gamma-ray emissions from these two pulsars and found the pulsed emissions from PSR J0540-6919. The total pulsed radiation in the X-ray/gamma-ray energy bands of PSR J0540-6919 is observed with the efficiency $\eta_{J0540} \sim 0.06$ (in 4π sr), which is about a factor of ten larger than $\eta_{Crab} \sim 0.006$ of the Crab pulsar. Although PSR J0537-6910 has the highest spin-down power among currently known pulsars, the efficiency of the observed X-ray emissions is about two orders of magnitude smaller than that of PSR J0540-6919. This paper mainly discusses what causes the difference in the radiation efficiencies of these three energetic Crab-like pulsars. We discuss electron/positron acceleration and high-energy emission processes within the outer gap model. By solving the outer gap structure with the dipole magnetic field, we show that the radiation efficiency decreases as the inclination angle between the magnetic axis and the rotation axis increases. To explain the difference in the pulse profile and in the radiation efficiency, our model suggests that PSR J0540-6919 has an inclination angle much smaller than the that of Crab pulsar (here we assume the inclination angles of both pulsars are $\alpha < 90°$). On the other hand, we speculate that the difference in the radiation efficiencies between PSRs J0537-6910 and J0549-6919 is mainly caused by the difference in the Earth viewing angle, and that we see PSR J0537-6910 with an Earth viewing angle $\zeta >> 90°$ (or $<< 90°$) measured from the spin axis, while we see PSR J0540-6919 with $\zeta \sim 90°$.

[1]School of physics, Huazhong University of Science and Technology, Wuhan 430074, China

[2]Department of Physics, The University of Hong Kong, Pokfulam Road, Hong Kong

1.   Introduction

PSRs J0537-6910 and J0540-6919 are energetic young pulsars in the Large Magellanic Cloud (hereafter LMC), and they were discovered by the X-ray observations (Seward et al. 1984; Marshall et al. 1998). The spin-down powers of PSRs J0537-6910 and J0540-6919 are $L_{sd} \sim 5 \times 10^{38}$erg s^{-1} and $\sim 1.5 \times 10^{38}$erg s^{-1}, respectively, which are similar to $L_{sd} \sim 4.5 \times 10^{38}$erg s^{-1} of the Crab pulsar. Among currently known pulsars, these three, PSR J0537-6910, Crab and J0540-6919, have the top three highest spin-down power (see Table 1). In this paper, "Crab-like pulsars" is used to refer to all three. The Fermi Large Area Telescope (hereafter Fermi-LAT) resolved the gamma-ray emissions from the two Crab-like pulsars in the LMC, and furthermore detected the pulsed emissions from PSR J0540-6919 (Ackermann et al. 2015).

PSR J0540-6919 (spin period $P_s = 0.05$s) is known as the "Crab-twin", because not only the spin-down parameters but also the properties of the pulsed emissions in multi-wavelength bands are similar to those of the Crab pulsar. First, Fermi-LAT found that the ratio of X-ray luminosity and > 0.1GeV gamma-ray luminosity is $L_X/L_\gamma \sim 1$, which is similar to $L_X/L_\gamma \sim 5$ for the Crab pulsar (Abdo et al. 2010). This feature is clearly distinct from $L_X/L_\gamma < 10^{-3} - 10^{-4}$ of the others (Abdo et al. 2013 for the Fermi-LAT pulsar catalog). Second, the pulse peaks in different wavelength bands are all in phase, just like the pulse profiles of the Crab pulsar. Furthermore, PSR J0540-6919 emits the giant radio pulses that appear at the positions of the pulse peaks in higher-energy bands (Johnston et al 2004). This property is also the same as for the Crab pulsar (Shearer et al. 2003). It is likely that there three features represent the nature of the pulsars with $L_{sd} > 10^{38}$erg s^{-1}.

While the Crab-like pulsars are similar in their spin-down properties, there are several remarkable differences in the observed radiation: (1) the pulse shape, and (2) the radiation efficiency, which is defined as the ratio of the radiation luminosity to the spin-down power $\eta \equiv L_{rad}/L_{sd}$. PSR J0540-6919 shows a broad pulse profile with a small dip at the center (Campana et al. 2008 for the X-ray pulse and Gradari et al. 2011 for the optical pulse), while the Crab pulsar shows a sharp double-peak structure with the phase separation of $\delta\phi \sim 0.4$ (Abdo et al. 2010). The integrated luminosity of the pulsed X-ray/gamma-ray emissions from PSR J0540-6919 is $L_{rad} \sim 10^{37}(d/50\text{kpc})^2$erg/s (in 4π sr), which is about a factor of 3 larger than that of the Crab pulsar, $L_{rad} \sim 3 \times 10^{36}(d/2\text{kpc})^2$erg/s. As a result, the radiation efficiency $\eta_{J0540} \sim 0.06$ of PSR J0540-6019 is a factor of ten larger than that of the Crab pulsar, $\eta_{Crab} \sim 0.006$. The Fermi-LAT confirmed that the luminosity of the non-thermal radiation from a pulsar tends to increase as $L_\gamma \propto L_{sd}^{1/2}$ (Abdo et al. 2013), which yields $\eta \propto L_{sd}^{-1/2}$. This empirical relation cannot explain the ratio $\eta_{J0540}/\eta_{Crab} \sim 10$. For PSR J0537-6910, the Fermi-LAT did not detect the pulsed emissions, and it measured the

spectrum fitted by a power-law function, suggesting the emissions originate from the pulsar wind and/or a supernova remnant. The pulsed X-ray emissions from PSR J0537-6910 were observed to be $F_X \sim 5 \times 10^{-13}$erg cm^{-2} s^{-1} in 2-10keV (Mineo et al. 2004), indicating the efficiency is $\eta_{J0537} \leq 10^{-3}$, which is much lower than those of the Crab and PSR J0540-6919. Since the distance to the Crab ($d \sim 2$kpc), and the LMC ($d \sim 50$kpc) are well determined, the uncertainty of the efficiency due to that is the distance should be small. The observed emission properties of the three energetic pulsars pose a challenge theoretically to see whether a unique model can explain all these systems.

Electron/positron acceleration and high-energy emission processes in the pulsar magnetosphere have recently been discussed within the framework of the slot gap model (Harding et al. 2008; Harding & Kalapotharakos 2015), outer gap model (Cheng et al. 2000, Hirotani 2015, Takata et al. 2016), current sheet of the force-free magnetosphere model (Spitkovsky 2006; Bai & Spitkovsky 2010), and pulsar wind model (Aharonian et al. 2012). In this paper, we will discuss the high-energy emission process within the framework of the outer gap accelerator model. For the Crab-like pulsars, the outer gap model has predicted that most of >GeV photons from the outer gap are converted into pairs by the pair-creation process and cannot escape from the light cylinder (see section 2, Cheng et al. 2000; Takata & Chang 2007; Tang et al. 2008). Synchrotron radiation and the inverse-Compton process of the secondary pairs can produce the observed emissions in the optical to TeV energy bands. The outer gap model predicts that the shape of the pulse profile is sensitive to the viewing angle and magnetic inclination angle measured from the spin axis. In the Fermi-LAT pulsar catalog (Abdo et al. 2013), $\sim 75\%$ of the sources show a double-peak structure in the pulse profile and $\sim 40\%$ show a wide phase (0.4$\sim$ 0.6) separation between the two peaks. The outer gap model explains the widely separated two peaks by assuming a larger magnetic inclination angle and a larger Earth viewing angle (Takata et al. 2011; Watters & Romani 2011). On the other hand, Takata & Chang (2007) explain the pulse profile of PSR J0540-6919 by a smaller inclination angle $\alpha \sim 30°$ and a larger viewing angle $\zeta \sim 90°$. The observed geometry of the pulsar wind tori also suggests the viewing angle $\zeta \sim 90°$ for PSR J0540-6919 (Ng & Romani 2004, 2008).

Previous studies of PSR J0540-6919 (Zhang & Cheng 2000; Takata & Chang 2007) mainly discussed the optical/X-ray emissions, since only the upper limit of the GeV flux had been reported before the launch of the Fermi. Hence, it is not obvious why the efficiencies of the observed radiations among the Crab-like pulsars are so different. In this paper, therefore, we will revisit the non-thermal emission process of the Crab-like pulsars with the outer gap model. In section 2, we will describe our theoretical model for the Crab-like pulsars. In section 3, we present our result of the fitting spectrum for PSR J0540-6919 and discuss the differences between the Crab and this pulsar. In section 4, we will discuss the emissions from

PSR J0537-6910.

2. Theoretical Model

We apply the calculation method developed in Takata et al. (2016), which solves the outer gap structure in the three-dimensional space with a rotating dipole magnetic field. They obtained the structure of the accelerating electric field and gap currents by solving the Poisson equation, and the continuity equations for the electrons and positrons and the pair-creation process. For the outer gap model, some electrons/positrons, which migrate along the magnetic field lines, should enter the outer gap from the gap boundaries and they initiate the gamma-ray radiation and subsequent pair-creation cascade processes. Takata et al. (2016) solved the pair-creation cascade inside the outer gap by assuming the number of the electron/positron injections at the gap boundaries, which is the crucial factor for control of the outer gap structure. We refer Takata et al (2016) for detailed calculations.

Takata et al. (2016) assumed that the outer gap structure is variable in time, rather than stationary, because of the time-dependent injection of the electrons/positrons at the gap boundaries. The model argued that the observed gamma-ray spectrum is a superposition of the emissions from different stationary gap structures with different injection rates at the gap boundaries. This dynamic model provides a better fit for the spectra of the Fermi-LAT pulsars. As we will argue later (see section 4), our model suggests that the observed emissions from the Crab-like pulsars are not from primary electrons/positrons accelerated in the outer gap, but from the secondary pairs created outside the gap, and therefore the dynamic behavior of the outer gap may be less important in explaining the pulsar's observed GeV spectra.

In our calculations, the model parameters that determine the gap dynamics are the inclination angle of the magnetic axis, the surface temperature of the neutron star, and the number of the electrons and positrons that enter the outer gap from the gap boundaries. We assume the magnetic inclination angle α less than 90° measured from the spin axis. For the rotator with a $\alpha < 90°$, the positrons and electrons can enter the gap from outside along the magnetic field lines by crossing the inner boundary (star side) and outer boundary (light cylinder side), respectively. We assume that the rate of the particle injection is constant over the inner and the outer boundaries. We parameterize the injection current in units of the Goldreich-Julian value and denote j_{in} and j_{out} as the normalized injection rates at the gap inner and outer boundaries, respectively. Our local model has to treat the injection currents (j_{in}, j_{out}) as the model fitting parameters. Takata et al. (2016) discussed the origin of the electrons/positrons that enter the outer gap at the gap boundaries.

In the outer gap, the positrons and electrons crossing the gap boundaries initiate the gamma-ray emission and a subsequent pair-creation cascade. The electrons/positrons are accelerated by the electric field parallel to the magnetic field and emit the gamma-rays via the curvature radiation process and/or the inverse-Compton scattering process. The emitted gamma-rays may be converted into pairs, by the pair-creation process, with the surface X-rays. The new pairs created in the gap are accelerated by the electric field and emit the curvature photons. The pairs created outside the gap lose their energy via the synchrotron radiation and the inverse-Compton scattering process. We denote as "primary" pairs as the electrons/positrons accelerated inside the gap, and as "secondary" pairs those produced outside the gap. Since no measurements on the surface temperature of the Crab-like pulsars have been made, we assume $T_s = 10^6$K as the temperature of the entire stellar surface.

The main difference from the calculation in Takata et al. (2016) is that the current model of the Crab-like pulsars takes into account emission from the pairs created outside the outer gap. The X-rays produced by the synchrotron radiation of the secondary pairs become the target soft-photon field for the photon-photon pair-creation process occurring outside the gap. One important difference in the circumstellar conditions between the Crab-like pulsars and other Fermi-LAT pulsars is the mean-free path of the pair-creation process between a > 1GeV photon and a background soft photon produced by the secondary pairs. The optical depth inside the light cylinder may be written down as

$$\tau_p(r) \sim rn_X\sigma_{\gamma\gamma} \sim 1 \left(\frac{L_X}{10^{35}\text{erg s}^{-1}}\right) \left(\frac{r}{\varpi_{lc}}\right)^{-1} \left(\frac{P_s}{0.05\text{s}}\right)^{-1} \left(\frac{E_X}{0.1\text{keV}}\right)^{-1}, \qquad (1)$$

where n_X is the number density of the soft photons, $\sigma_{\gamma\gamma} \sim 0.2\sigma_T$ is the cross-section, L_X is the X-ray luminosity, E_X is the energy of the soft photon, and $\varpi_{lc} = cP_s/2\pi$ is the light cylinder radius. The optical depth of the Crab-like pulsars is usually larger than unity with $L_X > 10^{35}$erg s^{-1}. For the Crab-like pulsars, therefore, most of the primary gamma-rays with an energy > 1GeV are absorbed by the pair-creation process and the secondary particles will emit the X-rays via synchrotron emission. This explains the ratio of X-ray and gamma-ray luminosity $L_X/L_{GeV} \sim 1$ for the Crab-like pulsars, where L_{GeV} is the *apparent* luminosity from the magnetosphere. For other Fermi-LAT pulsars, the mean-free path is of order $\tau_p \sim 10^{-3}$ with $L_X \sim 10^{32-33}$erg s^{-1}, and results in $L_X/L_{GeV} \sim 10^{-3}$.

To calculate the emission from the pairs produced outside the outer gap, we trace the propagation of the >GeV photons and the pair-creation rates on the trajectory. We calculate the pair-creation mean-free path by assuming the number density of the soft-photons inferred from the observations; that is,

$$\frac{dN_s(r)}{dE} = \left(\frac{d}{r}\right)^2 \frac{dN_{obs}}{dE}, \qquad (2)$$

where dN_{obs}/dE is the observed spectrum in the optical to hard X-ray energy bands and $d = 50$kpc is the distance to the LMC. The pitch angle, θ_p, of the newborn pairs produced outside the outer gap is calculated from

$$\cos\theta_p = \boldsymbol{b}(\boldsymbol{r}) \cdot \boldsymbol{n}_\gamma(\boldsymbol{r}_0), \qquad (3)$$

where $\boldsymbol{b}$ is the unit vector of the magnetic field, and $\boldsymbol{n}_\gamma$ is the propagation direction of the gamma-rays, and $\boldsymbol{r}$ and $\boldsymbol{r}_0$ represent the positions of the pair-creation and the radiation, respectively. The emission direction is calculated from $\boldsymbol{n}_\gamma(\boldsymbol{r}_0) = \beta_0\boldsymbol{b} + \boldsymbol{\beta}_{co}$, where $\boldsymbol{\beta}_{co}$ is the co-rotation velocity, and β_0 is calculated from $|\mathbf{n}_\gamma| = 1$. In the calculation, there is an uncertainty in the collision angle between the gamma-ray and magnetospheric soft photons. Since the latter are emitted by the secondary pairs, which has a pitch angle θ_p, we may assume a collision angle of $\theta_c \sim 2\theta_p$.

Grand based Cherenkov telescopes have observed the pulsed emissions up to ~ 1TeV from the Crab pulsar (Abdo et al. 2010; Aleksić et al. 2011, 2012, 2014; Aliu et al. 2008, 2011). The emissions between 10GeV and 1TeV are well fitted by a single power-law function. The standard curvature radiation process cannot easily explain the emissions above 100GeV from the Crab pulsar, which suggests the inverse-Compton scattering process inside the magnetosphere (Aleksić et al. 2011; Harding and Kalapotharakos 2015) or at the pulsar wind region (Aharonian et al. 2012). Within the framework of the outer gap scenario, the > 100GeV emissions of the Crab pulsar are explained by the emission process of TeV primary pairs and/or secondary pairs that were produced by the pair-creation process of the TeV photons from the inverse-Compton scattering process of the primary pairs. If the infrared (IR) photons from the secondary pairs enter the outer gap, they are up-scattered by ~ 1TeV electrons/positrons whose Lorentz factor is $\Gamma \sim 3 \times 10^7$, and become ~ 10TeV gamma-rays. Most of the TeV gamma-rays from the outer gap are absorbed by the soft photons outside the gap, and create ~ 1TeV electrons/positrons. The TeV secondary pairs also emit photons via synchrotron radiation and inverse-Compton scattering processes. Furthermore, the high-energy secondary photons also targets for the pair-creation. In this paper, we also examine the pair-creation cascade outside the outer gap which is initiated by the TeV gamma-rays from the outer gap, and we will discuss its contribution to the observed emissions of PSR J0540-6919. Since the IR photons are produced above the outer gap, we assume that they irradiate the outer gap at around the upper boundary, say $\sim 10\%$ of the gap thickness, with the number density estimated from equation (2). Since the emission direction of the IR will be related to the pitch angle in equation (3), we may roughly estimate the collision angle of the inverse-Compton scattering as $\cos\theta_{IR} \sim \boldsymbol{b} \cdot \boldsymbol{n}_\gamma$ at the emission point.

3. Results

3.1. Multi-wavelength spectrum

In this section, we apply the model to PSR J0540-6919. Since there are two kinds of the secondary pairs in our calculation, we define the terminology "low-energy secondary" which represents the pairs created by the primary curvature photons, and "high-energy secondary" for those created by primary TeV photons via the inverse-Compton scattering process.

Figure 1 shows the multi-wavelength spectrum of PSR J0540-6919 with the model fitting curves. In the figure, the dashed line shows the synchrotron and inverse-Compton scattering processes of the low-energy secondary pairs, and dashed-dotted line is the emissions from the high-energy secondary pairs. The results are for the inclination angle $\alpha = 10°$ and the observer viewing angle $\zeta = 80°$ (or 100°). In addition, we assume that the injection rate at the inner and outer boundaries is 1% of the Goldreich-Julian value, $j_{in} = j_{out} = 10^{-2}$. Figure 2 shows the intrinsic spectra for the curvature radiation (solid line) and inverse-Compton scattering process (dashed line) inside the gap.

As we can see in Figure 1, the emissions (dashed line) from the low-energy secondary pairs explain the observed emissions in the 100eV-1GeV energy bands. However, the calculated spectrum above 1GeV decays faster than the Fermi-LAT data. To reconcile with Fermi-LAT data above 1GeV, therefore, the present model predicts that the residual curvature emissions (thin solid line) and/or the emissions from high-energy secondary pairs (dashed-dotted line) contribute to the Fermi-LAT observations. In the current calculation, a fraction of high-energy photons (>10GeV) emitted by the secondary pairs created near the light cylinder can escape from the pair-creation process. As we will argue in section 4, the dynamic behavior of the outer gap discussed in Takata et al. (2016) will not be the main reason to explain the observed spectrum above the cut-off energy of PSR J0540-6919. With a small inclination angle $\alpha = 10°$, the calculated gamma-ray light curve (solid line in Figure 3) shows a broad pulse with two narrow peaks separated by $\delta\phi \sim 0.2$, which is consistent with the observations.

3.2. Luminosity versus Inclination angle

The Fermi-LAT observations found that the efficiency, η, of PSR J0540-6919 is about a factor of ten larger than the Crab pulsar, and this result is incompatible with the empirical relation $\eta \propto L_{sd}^{-1/2}$ of the Fermi-LAT pulsars (Abdo et al. 2013). Here we suggest the smaller magnetic inclination of PSR J0540-6919 causes the larger radiation efficiency than the Crab
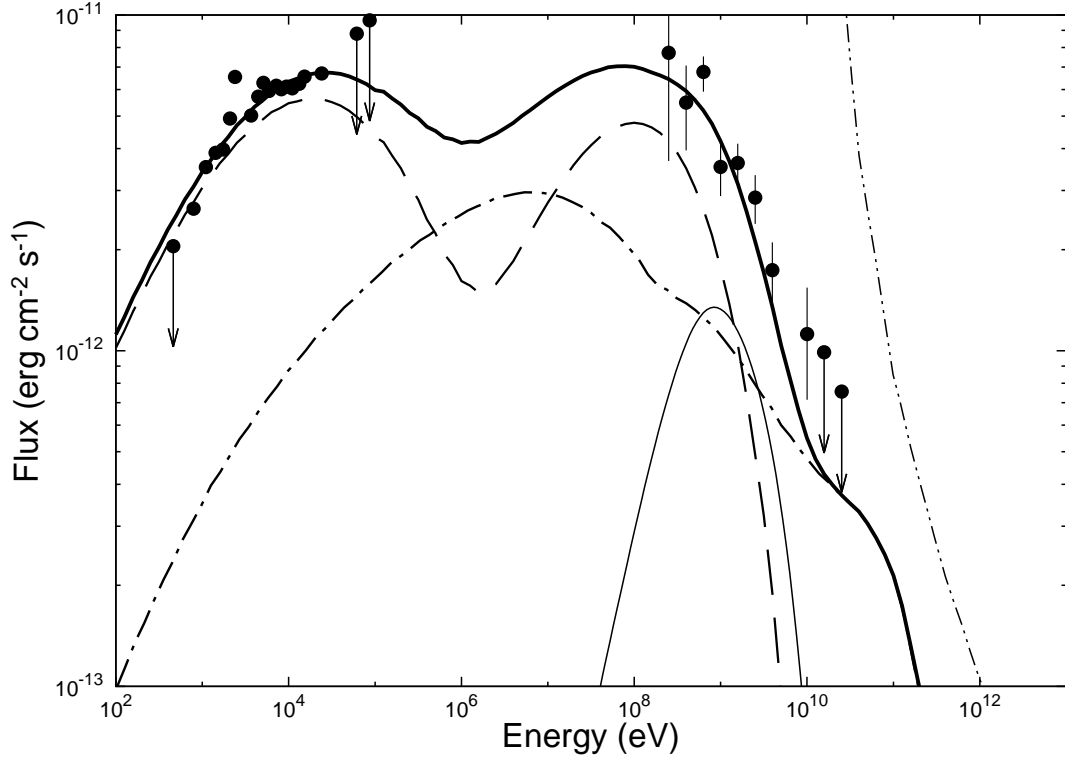
Fig. 1.— Multi-wavelength spectrum of PSR J0540-6919. The dashed line and dashed-dotted line represent the calculated spectra of the low-energy secondary pairs that are created by the primary curvature photons and the high-energy secondary pairs that were produced by primary TeV photons via the inverse-Compton process, respectively. The thin sold line is the spectrum of the residual curvature photons from the outer gap. The results are for the inclination angle $\alpha = 10°$ and viewing angle $\zeta = 80°$ (or 100°) and $j_{in} = j_{out} = 10^{-2}$. The dashed-double-dotted line is the expected sensitivity of the Cherenkov Telescope Array (Acharya et al. 2013). The observed X-ray data were taken from de Plaa et al. (2013). For Fermi-LAT data, we read the data from Ackermann et al. (2015) and multiplied 0.75 for estimating the pulsed fluxed, which is suggested in their paper.
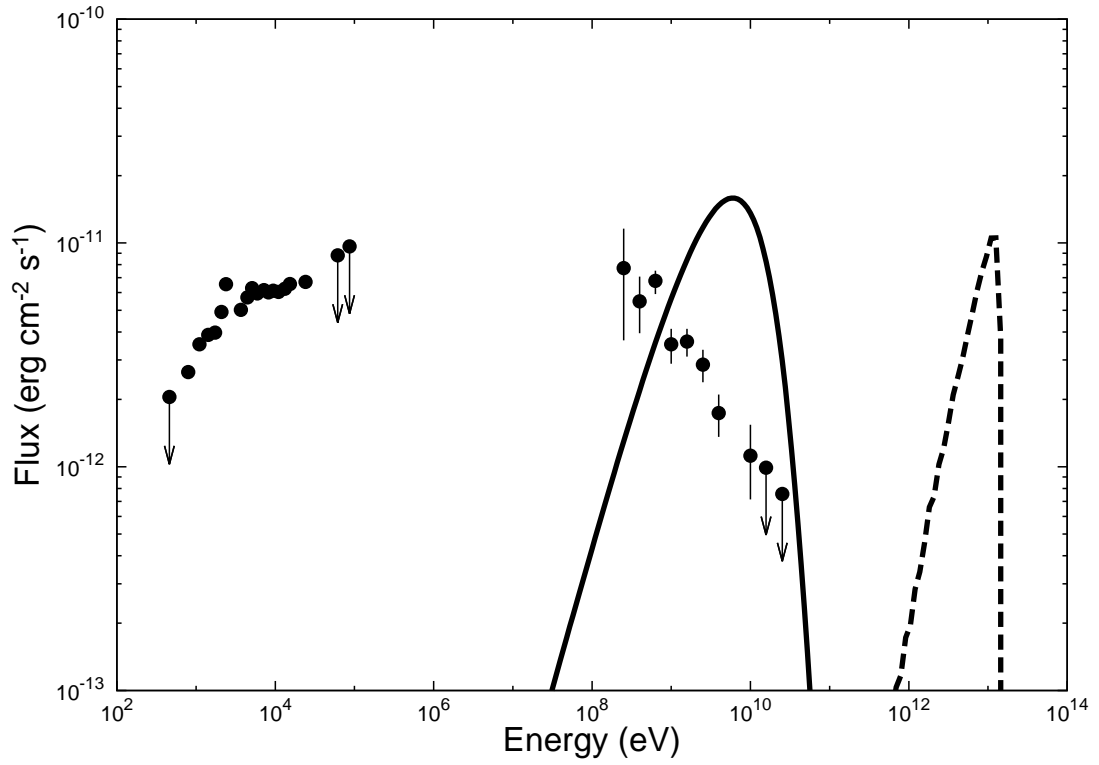
Fig. 2.— Intrinsic gamma-ray fluxes (measured on the Earth) from the outer gap. The solid and dashed lines show the spectra of the curvature radiation and the inverse-Compton scattering process, respectively.
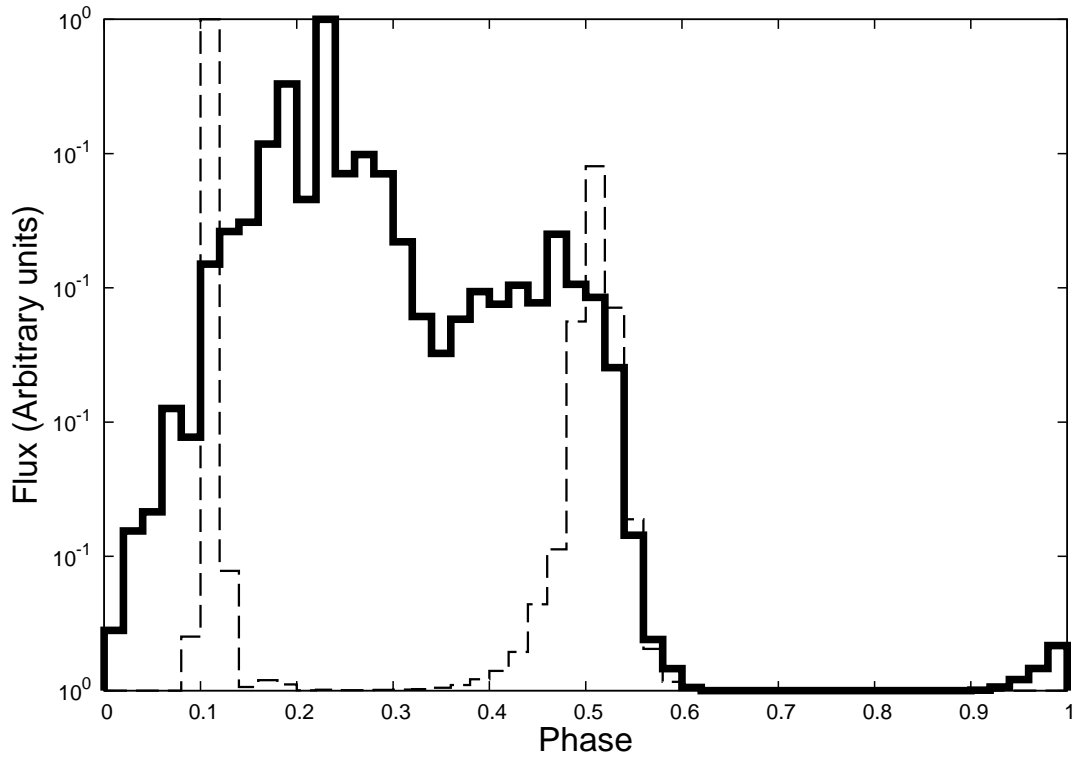
Fig. 3.— Calculated gamma-ray pulse profiles for the viewing angle $\zeta = 80°$. The inclination angle is $\alpha = 10°$ for solid line and $\alpha = 70°$ for dashed line, respectively.
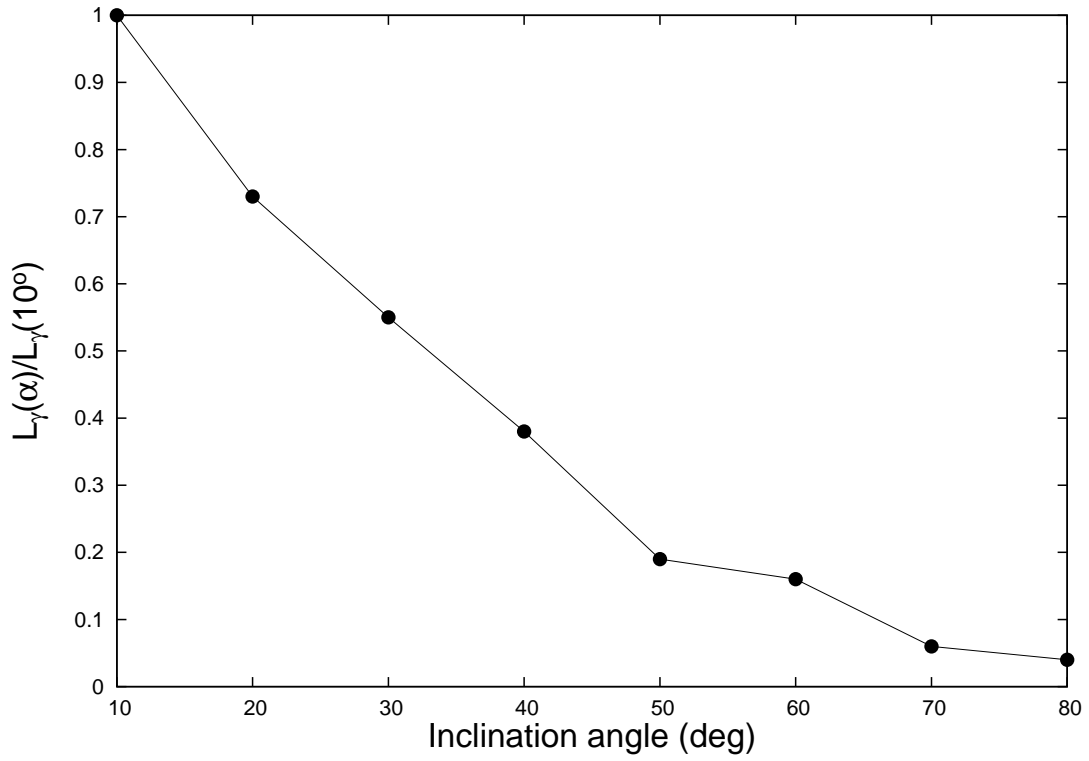
Fig. 4.— The calculated radiation luminosity with the function of the inclination angle. The vertical axis is normalized by the luminosity at $\alpha = 10°$. The results are for $j_{in} = j_{out} = 10^{-2}$.

pulsar, whose magnetic inclination angle will be relatively large.

Figure 4 shows the calculated gamma-ray luminosity as a function of the inclination angle. In the figure, the vertical axis is normalized by the calculated luminosity at $\alpha = 10°$. We find in the figure that the calculation luminosity tends to decrease as the inclination angle increases. In the current model, this dependency was caused by the dependency on (1) the position of the null charge surface of the Goldreich-Julian charge density and on (2) the maximum gap current on the inclination angle. The gap power depends on the thickness of the gap in the poloidal plane, and it decreases with decreasing of the thickness. The electrodynamics of the conventional gap models expects the relation that $L_\gamma \sim f_{gap}^3 L_{sd}$, where f_{gap} is defined by the ratio between the size of the outer gap measured on the stellar surface and the polar cap size (Takata et al. 2010). For the Crab-like pulsars, the outer gap size may be controlled by the mean-free path of the pair-creation process between the curvature photons and soft X-rays from the neutron star surface (Wang et al. 2010). Since the null charge surface on the last-open field lines approaches to the stellar surface with the increase of the inclination angle, the location of the outer gap is closer to the stellar surface for larger inclination angle. Since the number density of X-rays from the stellar surface is inversely proportional to the square of the radial distance, the pair-creation mean-free path inside the gap is shorter for the outer gap closer to the stellar surface. Hence, the outer gap becomes thinner and as a result the gap radiation power decreases with the increasing of the inclination angle.

In the current calculation, the pair-creation process inside the gap is occurring due to collision between GeV gamma-rays and surface X-rays. In this case, the mean free path of the pair-creation process at around the light cylinder is estimated as $\lambda(R_{lc}) \sim 100 R_{lc}$. With this mean-free path and the injection rate $j_{out} = 0.01$, the gap thickness is determined so as to produce $\sim 5 \times 10^4$ curvature photons inside the outer gap by one particle injected at the outer boundary, and thus to make ~ 100 of pairs by the pair-creation process inside the gap (see section 4). With a constant mean-free path $\lambda = 100_{lc}$, we find that the GeV photons have to travel a distance of $\sim 0.15 R_{lc}$ inside the gap to screen the gap. The mean-free path actually depends on the position as $\lambda(r) \propto r^2$. For a smaller inclination angle, because the null charger surface is close to the light cylinder, a constant mean-free path with $\lambda(r) = \lambda_0$ is a good approximation. For a larger inclination angle, on the other hand, the null charge surface is closer to the stellar surface and the radial dependency of the mean-free path becomes more important, indicating the average mean-free path is shorter. Therefore, the required travel distance of the gamma-rays to create ~ 100 pairs becomes shorter than $\sim 0.15 R_{lc}$ of the lower inclination case, and therefore the gap thickness reduces.

It has been suggested that the inner boundary of the middle part of the outer gap tends

to be shifted toward the stellar surface as the gap current increases. The model suggests that the inner boundary will touch on the stellar surface if the gap current is $j_{gap} \sim \cos \alpha$ in units of the Goldreich-Julian value (Takata et al. 2004), which decreases with increasing inclination angle. This is because the charge density that is created by the gap current at the inner boundary should match with the local value of Goldreich-Julian charge density, which on the polar cap region is $\sim \cos \alpha B_s/(P_s c)$. One may expect that if the inner boundary of the outer gap once touches on the stellar surface, the latter supplies copious particles to close the outer gap. Therefore, the gap luminosity decreases with increasing inclination angle.

As described in section 3.1, the smaller magnetic inclination angle of PSR J0540-6919 preferentially explains the observed small separation of the two peaks in the pulse profile. For a larger magnetic inclination angle ($\alpha \geq 50°$) and a viewing angle $\zeta \sim 90°$, the phase-separation between two peaks is $\delta\phi \sim 0.4 - 0.5$, as shown in Figure 3, and this would be the case for the Crab pulsar. We emphasize, therefore, that the smaller inclination magnetic angle of PSR J0540-6919 can explain both the higher radiation efficiency and the narrower phase separations of the two peaks than those of the Crab pulsar.

4. Discussion

4.1. PSR J0537-6910

Fermi-LAT resolved the gamma-ray emissions from the high spin-down powered pulsar, J0537-6910, in the LMC with a flux level of $F_\gamma \sim 10^{-11}$erg cm^{-2} s^{-1}. However, the pulsed emissions in Fermi-LAT data have yet to be confirmed, and the observed spectrum fitted by a single power-low function indicates the emissions to be from the pulsar wind nebula and/or a supernova remnant (Ackermann et al. 2015). Since PSR J0537-6910 has the largest spin-down power ($L_{sd} \sim 5 \times 10^{38}$ erg s^{-1}) and the strongest magnetic field at the light cylinder ($B_{lc} \sim 2 \times 10^6$G) among the known pulsars (see the ATNF pulsar catalog, Manchester et al. 2005), it is likely that this pulsar produces gamma-rays in the magnetosphere, and but they are buried under the background emission, or the gamma-ray beam is out of the line of sight. The observed emission properties of PSR J0537-6910 are very different from those of the Crab and J0537-6910; (1) the pulsed emissions have been discovered only in the X-ray bands, (2) the observed radiation efficiency in the X-rays is very low $\eta_X \sim 3 \times 10^{-4}$, and (3) the pulse width, ~ 0.2, in the X-ray bands (Marshall et al. 1998) is narrower than those of the other pulsars.

No detection of the pulsed emissions by the Fermi-LAT makes if difficult for us to discuss the electromagnetic spectrum in the wide energy bands, and to constrain the magnetic

inclination and the Earth viewing angle. However, we may expect that the radiation process of PSR J0537-6910 is similar to those of the Crab and J0540-6919, and we may assume that the flux level of the pulsed gamma-rays measured on the Earth is $F_\gamma \sim F_X$, which is the case for the Crab and PSR J0540-6919. Under those assumptions, the observed radiation efficiency will be of the order of $\eta_{J0537} \sim 10^{-3}$, which is about two orders of magnitude smaller than that of J0540-6919. As expected from Figure 4, we would say that it is difficult to explain $\eta_{J0540}/\eta_{J0537} \sim 100$ by the effect of the inclination angle. If both PSRs J0537-6910 and J0540-6919 have a viewing angle $\zeta \sim 90°$, it is also difficult to explain the difference in the pulse width with the difference in the inclination angle. We suggest therefore that the Earth viewing angle is very different between the two pulsars. Our model suggests that the Earth viewing angle of PSR J0540-6919 is close to $\zeta \sim 90°$ measured from the spin axis, which is also suggested by a study of the pulsar wind (Ng & Romani 2004,2008). Since most of the pairs inside the gap are created around the null charge surface, the outer gap emission is stronger for an Earth viewing angle of $\zeta \sim 90°$. As the viewing angle deviates from the $\zeta \sim 90°$, therefore, the observed gap emission rapidly decreases and hence the apparent radiation efficiency decreases (see figures 3 and 4 in Takata et al. 2011); at the same time, the pulse width becomes narrower. On these grounds, we speculate that the main reason for difference in the observed efficiencies and in the observed pulsed widths between PSRs J0540-6919 and J0537-6910 is the difference in the Earth viewing angle.

4.2. Dependency on j_{in} and j_{out}

In Figure 1, we assumed the same particle injection rates at the inner and outer boundaries. The assumption of equal injection rates at the gap boundaries is arbitrary, and it is not necessary for the real case. In the current *local* model, however, it would not be possible to consistently solve the injection particles at the gap boundaries, for which we would have to solve the global structure including the polar cap activities, outer gap activities, and pulsar wind region. To see the dependency on the choice of the injection current, we examined the case for $j_{in} = 0$ and $j_{out} = 0$, that is, no particles enter into the gap from the inner boundary (star side) or outer boundary (light cylinder side), respectively.

Figure 5 summarizes the dependency of the emissions from the low-energy secondary pairs on the injection currents j_{in} and j_{out}; the solid line, dashed line and dashed-dotted line are results for $(j_{in}, j_{out}) = (10^{-2}, 10^{-2})$, $(10^{-2}, 0)$ and $(0, 10^{-2})$, respectively. We find in the figure that the calculated spectra become harder for $j_{out} = 0$ (dashed line in Figure 5). This is related to the fact that most of the pairs are created by the inwardly propagating gamma-rays. Collision with the X-rays from the surface is a head-on process for inwardly

propagating gamma-rays, while it is tail-on process for outwardly propagating gamma-rays. Hence, the mean-free path of the former is shorter than that of latter, and most of the pairs are created by the inwardly propagating gamma-rays. This indicates that the gap size is mainly controlled by the pair-creation process of the inwardly propagating gamma-rays. For $j_{out} = 0$, therefore, the outer gap has to be thick to create enough pairs, and as a result the calculated spectrum becomes harder.

In our calculation, the gap structure is controlled by the magnitude of j_{out}, except for the case $j_{out} \ll j_{in}$. We quantitatively discuss how the gap size depends on the injection rate j_{out}. Since the gap thickness of the Crab-like pulsar is about 10% of the light cylinder radius, we can approximate that the propagation direction of the gamma-rays is the same as the direction of the particle's motion. Under this approximation, the evolution of the number density of the inwardly moving particles (electrons) and gamma-rays in the pair-creation region is described by

$$\frac{dn_-(s)}{ds} = \frac{g_-(s)}{\lambda(s)}, \tag{4}$$

and

$$\frac{dg_-(s)}{ds} = P_c n_-(s), \tag{5}$$

respectively, where s is the distance from the outer boundary, and n_- and g_- are number density and photon number density normalized by the Goldreich-Julian density, respectively. We ignore the effect of the pair-creation by the gamma-rays propagating outward. In addition, $\lambda(s)$ and P_c are the mean free path of the photon-photon pair-creation process and the rate of the curvature radiation. In the present calculation, since we assume the surface temperature $T_s \sim 10^6$K, the mean-free path inside the gap at the light cylinder is estimated as $\lambda_0 \sim 1/(\sigma_{\gamma\gamma} n_X) \sim 100 R_{lc}$, where we used $\sigma_{\gamma\gamma} = 0.2\sigma_T$ and $n_X \sim \sigma_{SB} R_s^2 T^3/(ck_B R_{lc}^2) \sim 3 \times 10^{14}$cm^{-3} with σ_{SB} being Stefan-Boltzmann constant. The rate of the curvature radiation is estimated as $P_c \sim 3 \times 10^4/R_{lc}(\Gamma/10^7)(R_c/R_{lc})^{-1}$, where R_c being the curvature radius, and Γ the Lorentz factor of the accelerated particles.

To solve the equations (4) and (5), we impose the boundary conditions as $n_-(0) = n_o$ and $g_-(0) = 0$, where $s = 0$ represents the outer boundary. We assume that the rate of the curvature radiation process, P_c, is constant along the magnetic field line. By assuming that mean free path is constant along the distance s from the outer boundary ($\lambda(r) = \lambda_0$), we find the solution that

$$n_-(s) = \frac{n_o}{2} \left(e^{c_1 s} + e^{-c_1 s} \right), \tag{6}$$

where $c_1 = (P_c/\lambda_0)^{1/2}$.

Since we consider the surface X-ray emission as the soft-photon field for the photon-photon pair-creation process inside the outer gap, the mean-free path will decrease as $\lambda \propto r^2$.
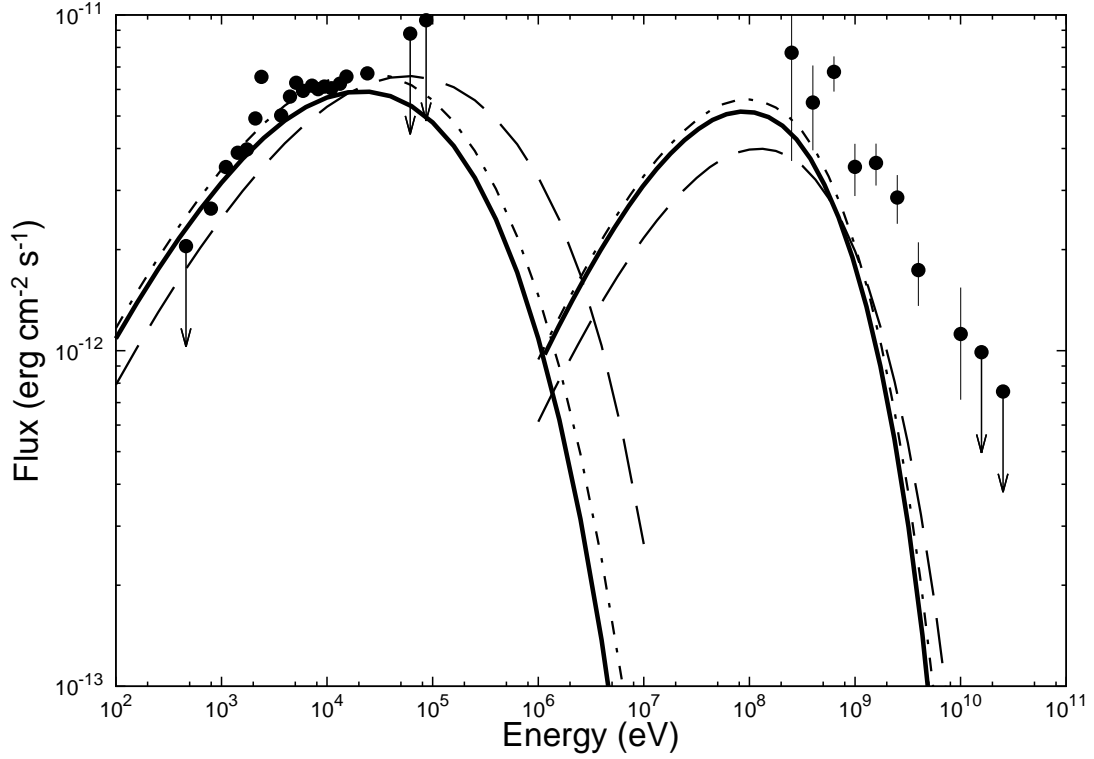
Fig. 5.— Multi-wavelength spectrum of PSR J0540-6919. The lines show the spectra of synchrotron radiation(lower energy part) and inverse-Compton scattering process (higher energy part) of the low-energy secondary pairs. The sold lines, dashed lines and dashed-dotted lines are result for $(j_{in}, j_{out}) = (10^{-2}, 10^{-2})$, $(10^{-2}, 0)$ and $(0, 10^{-2})$, respectively. In addition, we assume $\alpha = 10°$ and $\zeta = 80°$.
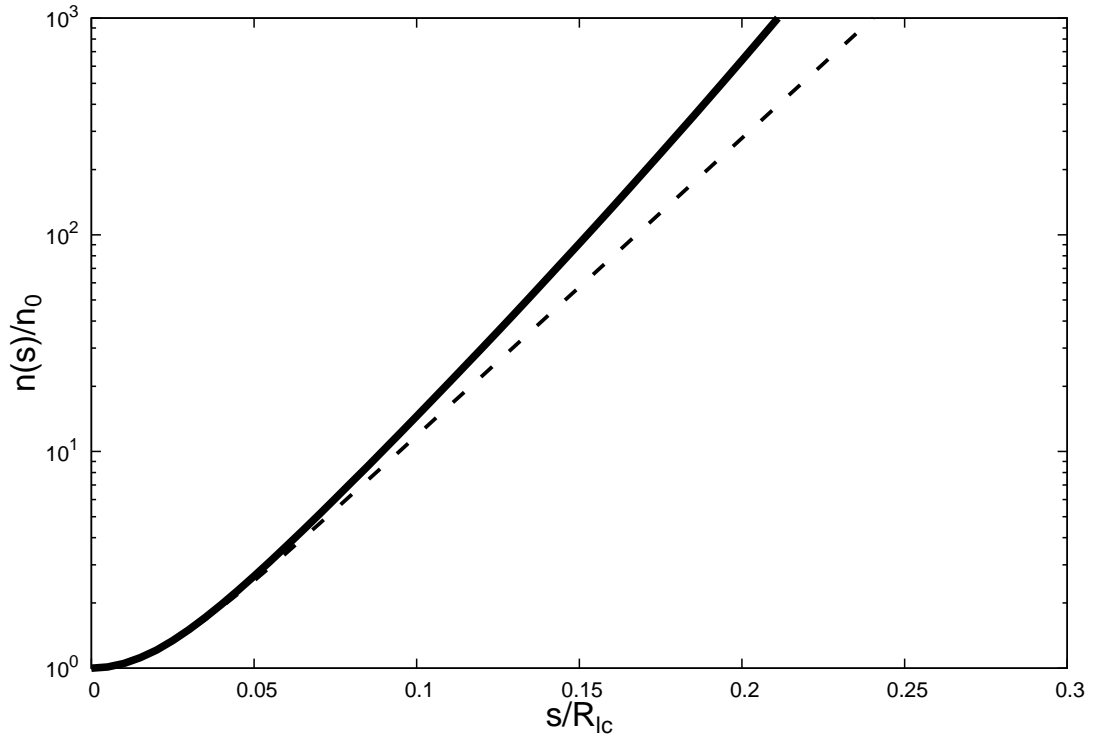
Fig. 6.— Evolution of the number of the inwardly moving particles in the pair-creation regions along the magnetic field line from the outer boundary. The solid and dashed line show the solutions for the pair-creation mean free path of $\lambda \propto (1-s/R_{lc})^2$ (7) and λ=constant (6), respectively.

To take into account this effect, we explore the solution with the mean-free path in the form $\lambda(s) = \lambda_0(1 - s/R_{lc})^2$. The solution becomes

$$n_-(s) = \frac{n_o}{b} \left[a_+ \left(1 - \frac{s}{R_{lc}} \right)^{a_+ - 1} - a_- \left(1 - \frac{s}{R_{lc}} \right)^{a_- - 1} \right], \tag{7}$$

where $a_\pm = (1 \pm b)/2$ with $b = \sqrt{1 + 4P_c R_{lc}^2/\lambda_0}$. Figure 6 shows the evolution of the ratio of the local number density and that at the outer boundary of the inwardly moving particles, $n(s)/n_o$, as a function of the distance from the outer boundary. The solid and dashed lines are solutions given by equations (7) and (6), respectively; here we adopted $P_c = 10^5/R_{lc}$ and $\lambda_0 = 10^2 R_{lc}$.

We can find in the figure that the multiplicity of the particles injected at the outer boundary becomes ~ 100 if the gamma-rays travel $\sim 0.15 R_{lc}$ from the outer boundary. This suggests that if the injection rate at the boundary is 1% of the Goldreich-Julian value (that is, $j_{out} = 0.01$), the number density becomes the Goldreich-Julian value after the gamma-ray travels $\sim 0.15 R_{lc}$ in the outer gap and the created pairs will significantly screen the accelerating electric field. This is consistent with the gap structure solved in this paper. Figure 6 also indicates that for a smaller injection rate, the gamma-rays have to travel a greater distance to achieve the Goldreich-Julian number density of the pairs by the pair-creation, and hence the gap size becomes larger.

As Figure 1 shows, the current model with using constant injection rate (j_{in}, j_{out}) predicts that the residual curvature radiation of the primary particles and/or the emissions from the high-energy secondary pairs can explain the observed emissions above 1GeV. Takata et al. (2016), on the other hand, argued that sub-exponential decays of the GeV spectra of the Fermi-LAT pulsars reflect the time-dependent emission process of the outer gap. They proposed that the injection rate at the gap boundaries is time-dependent variable and the observed gamma-ray spectrum is emitted from different gap structures with different injection rates. In the model, the observed spectrum was fitted better as the superposition of several power-law plus exponential cut-off functions with varying the cut-off energy, for which the different components are produced at the different injection rates at the gap boundaries.

We discuss the shape of the observed GeV spectrum of PSR J0540-6191 by the Fermi-LAT with the dynamics model in Takata et al. (2016). We find however that the calculated GeV spectra do not greatly affect the assumed extent of injection rate at the gap boundaries. This is because the GeV gamma-rays observed on the Earth do not come from the primary pairs in the gap, but the secondary pairs that are decelerated by the radiation process. Figure 7 shows the spectra of the emissions from the low-energy secondary pairs calculated with different injection rates; $j_{in} = j_{ou} = 10^{-2}$ (solid line), 10^{-3} (dashed line) and 10^{-4}

(dotted line). We can see that the hardness (peak energy) of the "synchrotron emissions" (low-energy component) increases with decreasing of the injection rate. This is because the gap thickness increases and hence the electric field in the gap becomes stronger as the injection rate decreases. As a result, the energy distribution of the low-energy secondary pairs that emit synchrotron photons becomes harder for a gap with a smaller injection rate. On the other hand, the energy peak of the spectra by "inverse-Compton scattering" (high-energy component) does not greatly depend on the injection rate. This is because the synchrotron cooling is more important for the particles with a Lorentz factor $\Gamma > 200$ than the radiation cooling, due to the inverse-Compton scattering. As Figure 7 shows, therefore, the energy peak of the inverse-Compton scattering of low-energy secondary pairs always appears around $\sim 100 \text{MeV}$, regardless of the injection rates. As a result, it is obvious from Figure 7 that even if we superpose the emissions calculated with different injection rates, the combined spectrum decays faster and still has a large discrepancy with the Fermi-LAT spectrum above 1GeV. On these grounds, we conclude that the residual curvature photons and/or the emissions from the high-energy secondary pairs contribute to the observed emissions above 1GeV.

In summary, we discussed the gamma-ray emissions from the Crab-like pulsars, PSRs J0537-6910 and J0540-6919, in the LMC. The pulsed emissions from PSR J0540-6919 is observed to have an efficiency that is a factor of ten larger than that of the Crab pulsar. By solving the electrodynamics of the outer gap accelerator, we concluded that the difference in the radiation efficiencies of PSR J0540-6919 and the Crab pulsar is caused by the difference in the inclination angle. Inferred from the observed X-ray emissions, the radiation efficiency of PSR J0537-6910 is about two orders of magnitude smaller than that of PSR J0540-6919. Because of the very narrow X-ray pulse and low radiation efficiency of PSR J0537-6910, we suspect that the Earth viewing angle of PSR J0537-6910 greatly deviates from $\zeta \sim 90°$, which is the case for the Crab and PSR J0540-6919.

REFERENCES

Abdo, A. A.; Ackermann, M.; Ajello, M.; Atwood, W. B.; Axelsson, M.; Baldini, L.; Ballet, J. et al., 2010, ApJ, 708, 1254
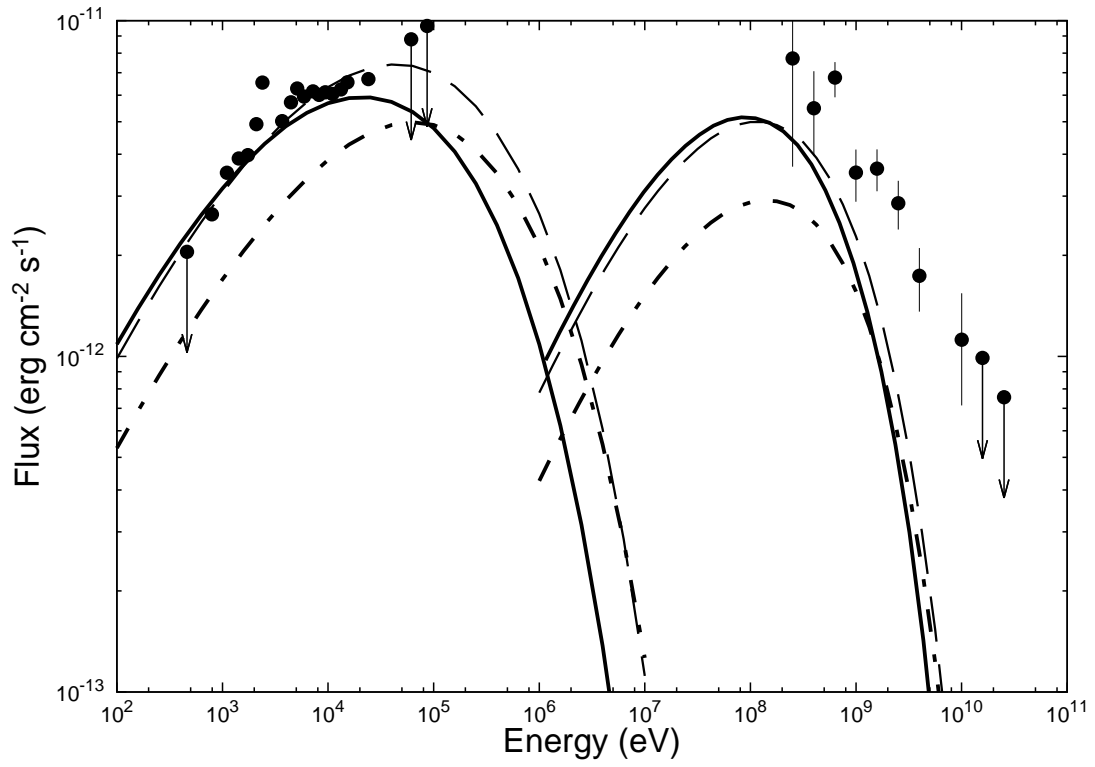
Fig. 7.— Same as Figure 5, but $(j_{in}, j_{out}) = (10^{-2}, 10^{-2})$ for solid lines, $(10^{-3}, 10^{-3})$ for dashed lines and $(10^{-4}, 10^{-4})$ for dashed-dotted lines.

Abdo, A. A.; Ajello, M.; Allafort, A.; Baldini, L.; Ballet, J.; Barbiellini, G.; Baring, M. G.; Bastieri, D., et al., 2013, ApJS, 208, 17

Acharya, B. S.; Actis, M.; Aghajani, T.; Agnetta, G.; Aguilar, J.; Aharonian, F.; Ajello, M.; Akhperjanian, A. et al., 2013, APh, 43, 3

Ackermann, M.; Albert, A.; Baldini, L.; Ballet, J.; Barbiellini, G.; Barbieri, C.; Bastieri, D.; Bellazzini, R., et al., 2015, Sci, 350, 801

Aharonian, F. A.; Bogovalov, S. V.; Khangulyan, D., 2012, Nature, 482, 507

Bai, X.-N.; Spitkovsky, A., 2010, ApJ, 715, 1282

Aleksić et al. 2011, ApJ, 742, 43

Aleksić et al. 2012, A&A, 541, 13

Aleksić et al. 2014, A&AL, 565, 12

Aliu, E., et al., 2008, Sci, 322, 1221

Aliu, E., et al., 2011, Sci, 334, 69

Campana, R.; Mineo, T.; de Rosa, A.; Massaro, E.; Dean, A. J.; Bassani, L., 2008, MNRAS, 389, 691

Cheng, K. S.; Ruderman, M.; Zhang, L., 2000, ApJ, 537, 964

de Plaa, J.; Kuiper, L.; Hermsen, W., 2003, A&A, 400, 1013

Gradari, S.; Barbieri, M.; Barbieri, C.; Naletto, G.; Verroi, E.; Occhipinti, T.; Zoccarato, P.; Germanã, C., 2011, MNRAS, 412, 2689

Harding, A.K.; Kalapotharakos, C., 2015, ApJ, 811, 63

Harding, A. K.; Stern, J. V.; Dyks, J.; Frackowiak, M., 2008, ApJ, 680, 1378

Hirotani, K., 2015, ApJL, 798, 40

Johnston, Simon; Romani, Roger W.; Marshall, F. E.; Zhang, W., 2004, MNRAS, 355,31

Manchester, R. N.; Hobbs, G. B.; Teoh, A.;Hobbs, M., Astron. J., 129, 1993-2006 (2005) (astro-ph/0412641)

Marshall, F. E.; Gotthelf, E. V.; Zhang, W.; Middleditch, J.; Wang, Q. D., 1998, ApJ, Letter, 499, 179

Mineo, T.; Cusumano, G.; Massaro, E. 2004, Nuclear Physics B Proceedings Supplements, Volume 132, p. 632-635

Ng, C.-Y.; Romani, Roger W., 2008, ApJ, 673, 411

Ng, C.-Y.; Romani, Roger W., 2004, ApJ, 601, 479

Renaud, M.; Marandon, V.; Gotthelf, E. V.; et al. 2010, ApJ, 716, 663

Seward, F. D.; Harnden, F. R., Jr.; Helfand, D. J., 1984, ApJ, Letter, 287, 19

Shearer, A.; Stappers, B.; O'Connor, P.; Golden, A.; Strom, R.; Redfern, M.; Ryan, O., 2003, Sci, 301, 4923

Spitkovsky, A., 2006, ApJ, Letter, 648, 51

Takata, J.; Ng, C. W.; Cheng, K. S., 2016, MNRAS, 455, 4249

Takata, J.; Wang, Y.; Cheng, K. S., 2011, MNRAS, 415, 1827

Takata, J.; Wang, Y.; Cheng, K. S., 2010, ApJ, 715, 1318

Takata, J.; Chang, H.-K., 2007, ApJ, 670, 67

Takata, J.; Shibata, S.; Hirotani, K., 2004, MNRAS, 348, 241

Tang, Anisia P. S.; Takata, J.; Jia, J. J.; Cheng, K. S., 2008, ApJ, 676, 562

Wang, Y.; Takata, J.; Cheng, K. S., 2010, ApJ, 720, 178

Watters, Kyle P.; Romani, Roger W., 2011, ApJ, 727, 123

Zhang, L.; Cheng, K. S., 2000, A&A, 363, 575

PSRs	P_s	$L_{sd,38}$	$B_{lc,6}$	d_{kpc}	η_x	η_γ
J0537-6910[a]	0.016	4.9	2.07	50	3×10^{-4}	-
Crab[b]	0.033	4.5	0.96	2	5×10^{-3}	10^{-3}
J0540-6919[c]	0.05	1.5	0.36	50	0.024	0.038
J1813-1749	0.045	0.56	0.25	4.7	-	-
J1400-6325[d]	0.03	0.51	0.35	7	10^{-3}	$< 1.5 \times 10^{-3}$

Table 1: The five most energetic pulsars: From the left to the right columns, pulsar name (PSR), rotation period (P_s) in units of second, spin down age ($L_{sd,38}$) in units of 10^{38}erg s^{-1}, the magnetic field strength at the light cylinder ($B_{lc,6}$) in units of 10^6G, distance to the source (d_{kpc}) in units of kpc, X-ray efficiency and gamma-ray efficiency (in 4π radian). a; the X-ray efficiency in 2-10keV energy bands (Mineo et al. 2004). b; the X-ray efficiency in 0.3-10keV and gamma-ray efficiency above 100MeV (Abdo eta l. 2013). c; the X-ray efficiency calculated with "absorbed" fluxes in 2-10keV and 20-100keV (Campana et al. 2008) and gamma-ray efficiency above 100MeV (Ackermann et al. 2015). d; the efficiency in 20-100keV, including pulsar and PWN and upper limit of gamma-ray efficiency (Renaud et al. 2010 and reference therein).